J Mater Sci (2008) 43:3539–3552
DOI 10.1007/s10853-008-2550-0

In situ high-temperature electron microscopy of 3DOM cobalt, iron oxide, and nickel

Christopher F. Blanford · C. Barry Carter · Andreas Stein

Received: 8 September 2007 / Accepted: 11 February 2008 / Published online: 22 March 2008

Abstract High-temperature electron microscopy was used to follow how the structure of two specimens of three-dimensionally ordered macroporous (3DOM) materials, also known as inverse opals, and one specimen of a precursor to a 3DOM material changed with temperature. The change in grain size with temperature of 3DOM cobalt and 3DOM iron oxide (as magnetite) was monitored in situ in the TEM by heating in stages to 900 and 1,000 °C, respectively. The two materials studied by TEM showed contrasting grain growth behavior. For 3DOM cobalt, carbon surrounding the nanometer-size grains led to slower grain growth in thinner sample areas than in areas in closer contact with other grains; a bimodal grain-size distribution was observed after heating above 700 °C for 90 min. The grains of the 3DOM iron oxide had no carbon coating and coarsened more evenly to give a unimodal size distribution. Line scans from selected-area diffraction (SAD) patterns were used for phase analysis and showed that traces of cobalt oxide present in the 3DOM cobalt sample at room temperature disappeared when the sample was heated above 500 °C. The transformation of a 3DOM precursor material, nickel(II) oxalate–polystyrene (PS) latex composites, was followed in situ by variable-temperature environmental scanning electron microscopy (ESEM) from room temperature to ca. 700 °C in 0.5–0.7 kPa O_2. The ESEM examination of the 3DOM precursors permitted real-time observation of the polymer template decomposition and the shrinkage that occurs upon calcination of these precursor materials.

C. F. Blanford (✉) · A. Stein
Department of Chemistry, University of Minnesota, 207 Pleasant Street SE, Minneapolis, MN 55455-0431, USA
e-mail: blan0069@tc.umn.edu;
christopher.blanford@chem.ox.ac.uk

C. F. Blanford
University of Oxford, Inorganic Chemistry Laboratory, South Parks Road, Oxford OX1 3QR, UK

C. B. Carter
Department of Chemical, Materials & Biomolecular Engineering, University of Connecticut, 191 Auditorium Road Unit 3222, Storrs, CT 06269-3222, USA

Introduction

Three-dimensionally ordered macroporous (3DOM, to rhyme with "freedom") materials, also known as inverse opals, are porous solids possessing uniform, spheroidal voids that are ordered in three dimensions [1–3]. They are generated by creating an inverse replica of three-dimensional opal-like colloidal crystals and can be of virtually any composition [4, 5]. The repeat distance between pores in these remarkably open structures is typically on the order of 100 nm to 1 μm which allows 3DOM materials to interact strongly with visible light [6, 7]. This interaction, plus their flexible and straightforward synthesis, has led to a surge of interest into 3DOM materials for photonic band gap devices, which can control the flow of photons in a similar manner to which semiconductors can control the flow of electrons [8], as well as numerous other applications that take advantage of the porosity of 3DOM materials [4, 5]. The potential significance of 3DOM materials as photonic devices relies on predictable control of a material's microstructure. The use of 3DOM products as catalysts or supports requires an understanding of the changes that the microstructure undergoes in different conditions. This work explores two promising methods of in situ high-temperature electron microscopy which can be

used to monitor the structural evolution of 3DOM materials as the temperature is varied.

Structurally, 3DOM materials fit in among other ordered porous materials such as zeolites or M41S materials (such as MCM-41) [9]. According to the IUPAC classification [10], the pores in 3DOM materials occupy the category of macropores, those larger than 50 nm in diameter. Synthetically, 3DOM materials are similar to zeolites and M41S, but are templated by colloidal crystals rather than small molecule structure-directing agents [11] or surfactant micelles [12]. Colloidal crystals are ordered, self-assembled structures in which the component particles are arranged on regular lattice points in the same way that atoms are arranged in a crystal, with the "atoms" in this case being several orders of magnitude larger [13, 14]. In 3DOM materials, a fluid precursor (such as a sol [1–3], salt solution [15], colloidal suspension [16], or reactive gas [17, 18]) fills the spaces between the opaline template. An alternate method involves creating colloidal crystals from pre-made core-shell structures [19]. If necessary, the precursor is transformed into a stable solid. The final step is to remove the template chemically or thermally to create the inverse structure.

The high degree of ordering, flexible composition, and the spacing between pores are central to the enormous interest in 3DOM materials for optical applications, particularly for photonic band gap materials or photonic crystals. These are periodic structures made of dielectric materials, metals, or a combination of both that affect the propagation of electromagnetic waves (including visible light) [8, 20, 21]. The optical properties of opals are intimately connected to the arrangement of the spheres [22–24]; similarly, the periodic arrangement of voids in a 3DOM structure affects its photonic properties [3, 25]. Additionally, the widely adaptable synthesis of 3DOM materials means that the composition of the final product can be finely adjusted to control electronic and ionic transport properties, bioactivity, porosity and specific surface area, catalytic behavior, sensing ability, sorption properties, thermal emission, and the dielectric/refractive index contrast (see, for example, recent reviews [4, 5, 26]). The last parameter, the amplitude of the periodic variation in refractive index, is crucial for photonic applications because it determines the strength of the photonic interaction [27]. Thus, a critical feature of the processing is that the colloidal crystal template, which forms the initial "scaffold" for these structures, must be removed, and then the walls of the voids must be transformed into reasonably stable solids with a grain size much smaller than the wavelength of light on which it should operate.

While many techniques are available for the characterization of solid-state materials, including powder X-ray diffraction (PXRD), solid-state nuclear magnetic resonance (NMR) spectroscopy, and gas physisorption or chemisorption, these techniques analyze the average or bulk properties. For the characterization of discrete areas, electron microscopy is an essential tool and plays a vital role in the characterization of 3DOM products [28]. For example, PXRD may show the presence of several phases; selected-area diffraction (SAD) can show which phase or phases belong to the ordered structure. Moreover, the template removal (calcination) and grain growth processes can be studied in situ using a combination of scanning electron microscopy (SEM) and transmission electron microscopy (TEM) as illustrated in the present paper.

Both techniques were explored in this work because of the complementary information that they provide. High-temperature TEM analysis of samples of 3DOM materials prepared ex situ allows high-resolution monitoring of grain sizes and interfaces; however, only areas $\sim 1\ \mu m^2$ or smaller can be monitored, and the samples must be electron transparent. In contrast, high-temperature ESEM monitoring of the degradation of 3DOM precursors allows bulk, electron-opaque samples to be analyzed at conditions more closely matching those used during template removal, but at the expense of spatial resolution.

There are few examples of the use of high-temperature TEM (HT-TEM) to examine nanostructured materials. These include studies of gold nanoparticles on multiwall carbon nanotubes [29] and ceria [30], titanate nanotubes [31], TiN/AlN superlattices [32], and phase diagrams of metal nanoparticles [33, 34]. High-temperature *environmental* TEM, in which the sample is kept close to atmospheric pressure (rather than the usual high-vacuum conditions of the TEM column), has been pioneered by Gai [35], and is well illustrated by her work on defect motion in vanadyl phosphate catalysts [36].

High-temperature and environmental SEM has been used to a lesser extent than HT-TEM to study ceramics in such applications as monitoring cement hydration [37, 38], monitoring the crystallochemical and morphological evolution of a system of nanostructured zinc oxide and sodium chloride [39], and examining the interactions of hydrogen sulfide with a yttria-doped zirconia–nickel cermet [40].

This current work augments these existing studies and extends high-temperature microscopy to the intensively researched porous, nanostructured 3DOM materials by highlighting the techniques' utility as a diagnostic tool for the material's microstructure.

Experimental

General synthesis

Samples of 3DOM materials were formed from polymer colloidal crystals infiltrated with metal oxalates [2, 15,

41–43] or metal alkoxide sols [2, 41]. Aqueous suspensions of uniformly sized polystyrene (PS) and poly(methyl methacrylate) (PMMA) latex spheres were synthesized by emulsifier-free emulsion polymerization [44–47]. The solid colloidal crystal template was formed by centrifugation of latex suspension at 670*g* for 1–2 d, after which the supernatant liquid was decanted and the pellet allowed to dry overnight in ambient conditions. The colloidal crystal pellet was then mixed with the metal oxalate precursor solution; excess precursor solution was removed from the composite by vacuum filtration. Alternatively, the colloidal crystal pellet was placed on a filter paper on the vacuum filtration apparatus, lightly crushed to produce millimeter-size latex chunks, and a metal alkoxide sol was allowed to filter through. The latex polymer was decomposed by heating the composite, typically in a tube furnace with a slow stream of gas flowing over it. The choice of temperature and gas composition (i.e., oxidizing, reducing, or inert) greatly affected the composition and microstructure of the final product [15, 42, 43].

Material specifics

3DOM iron oxide was synthesized from iron(II) oxalate dihydrate (Aldrich) [15]. To 5 mL of water, 2 g of iron(II) oxalate and 2 g of oxalic acid were added. The iron(II) was oxidized to iron(III) by dropwise addition of aqueous hydrogen peroxide (30%) until all the solids dissolved, then 5 mL of ethanol was added to the solution. Solid PS colloidal crystal ($\sim$2 g) was soaked in the mixture for 3–5 min, then the excess solution was removed. The composite was dried in an oven in air at 65 °C for 1 h. The template was removed by heating in air for 6 h at 400 °C at 1 °C min^{-1}. The product phase was α-Fe_2O_3/hematite, as identified by powder X-ray diffraction (PDF No. 33-0664) [48].

3DOM iron was made by a similar procedure, but used a PMMA template and was heated in air for 3 h at 300 °C then hydrogen for 1 h at 400 °C at 2 °C min^{-1}.

3DOM cobalt metal was synthesized from 2 g of cobalt(II) acetate tetrahydrate (Matheson, Coleman & Bell) added to 10 mL of glacial acetic acid. Excess solid was filtered off to leave a saturated solution. The solution was allowed to penetrate the PMMA colloidal crystal and was dried in the same way the 3DOM iron oxide was. The dried composite was soaked in 10 mL of aqueous oxalic acid solution ($\sim$30 g in 100 mL water) for 5–10 min to precipitate cobalt oxalate within the template's pores. The sample was heated at 2 °C min^{-1} in flowing nitrogen for 3 h at 300 °C then 3 h more at 400 °C to decompose the PMMA and convert the cobalt oxalate to cobalt metal and carbon dioxide [43]. Elemental analysis indicated that 20 wt% carbon remained after calcination.

The nickel(II) oxide–PS sample examined in situ by ESEM was made in an identical fashion, but using nickel(II) acetate tetrahydrate (Acros) as precursor salt [42].

Characterization

Transmission electron microscopy was carried out on a Philips CM30 Scanning Transmission Electron Microscope equipped with a LaB_6 filament and operating at 300 kV. Images were recorded on a thermoelectrically cooled, 1 megapixel Gatan Multiscan slow-scan charge-coupled device (CCD). Specimens for observation in the TEM were supported on holey carbon films mounted on 3.0 mm 300-mesh nickel grids (Electron Microscopy Sciences) and held on a single-tilt heating stage (Gatan). Copper grids were not used because they can form a diffusion bond to the specimen holder at high temperatures. The plastic coating supporting the holey carbon film was removed by holding the grids with anticapillary tweezers and dipping them in chloroform and acetone before wicking away the excess solvent on lint-free tissue. Samples were dispersed in ethanol by ultrasonication: 5–20 mg of powdered sample was dispersed in 2–4 mL of ethanol and sonicated for up to 1 min. Five drops of this suspension were dripped onto a prepared holey carbon grid sitting on absorbent lint-free paper towel.

Areas chosen for observation in the TEM were in contact with the metal bars of the support grid to allow thermal conduction from the holder to the 3DOM cobalt structure. 3DOM structures that were not in contact with the metal grid bar changed very little throughout the course of each measurement, indicating little radiative or conductive heat transfer from the holder or the grid to the sample. No convective heat transfer could occur in the high-vacuum environment of the TEM column. The heating profiles for the 3DOM cobalt and 3DOM iron oxide samples are shown in Tables 1 and 2, respectively. The temperature stabilized less than 1 min after it was changed.

Environmental scanning electron microscopy (ESEM) was carried out on an Electroscan ESEM operating at 15 kV in 4–5 Torr (0.5–0.7 kPa) oxygen gas at temperatures from ambient to 700 °C. The sample was set in an alumina crucible above a resistive heating element and a thermocouple. The temperature was controlled by manually adjusting the current flowing through the heater.

The use of selected-area electron diffraction in the TEM for identification of crystalline phases [49]

Selected-area electron diffraction was used to analyze crystalline phases of 3DOM materials. Measurements were carried out electronically in a three-step process. First, a line-scan profile (LSP) from a 10- to 20-pixel-wide cross

Table 1 Heating profile for 3DOM cobalt

Time (min)	Temperature (°C)
0	19 → 500
16	→600
52	→700
71	→800
96[a]	→900
100	→19

[a] The grid ruptured at 96 min, ending the measurement

Table 2 Heating profile for 3DOM iron oxide

Time (min)	Temperature (°C)
0	19 → 650
45	→750
70	→1,000
71	→950
141	→19

section was taken from the 16-bit CCD image of the diffraction pattern. This LSP was centered so that peaks were equidistant from the center. A swath was chosen to average out any local variations in the ring intensity. Wider swaths were used on samples with larger average grain sizes, and thus, less uniform diffraction rings. Next, the background of scattered electrons was subtracted from the spectrum. The background was modeled by a non-linear least-squares fit to Eq. 1.

$$I = Ad^B, \tag{1}$$

where I is the average number of counts in the LSP, d is the d-spacing of the line in pm, and A and B are fitting constants. The background fitting parameters for all the SAD patterns shown in this chapter are listed in Table 3. The region of the LSP that was fit was from about 30 pixels from the center to about 20 pixels from the first diffraction spot.

Finally, the spectrum was converted from reciprocal space to real space by the equation

Table 3 Empirical fitting parameters for SAD patterns

Figure	Material	Temperature	Pre-exponent A	Exponent B
3(d)	FeO_x	RT	0.1493	1.488
7(a)	Co/CoO	500 °C	0.1638	1.5250
7(b)	Co	602 °C	0.0294	1.7291
7(c)	Co	793 °C	0.1149	1.5483
7(d)	Co	882 °C	0.0186	1.8043
10(a)	Fe_2O_3	RT	0.1711	1.5839
10(b)	Fe_2O_3	650 °C	0.0040	1.8191
10(c)	Fe_2O_3	750 °C	0.0021	1.8678

$$d = \frac{\lambda L}{R}, \tag{2}$$

where d is the spacing between lattice planes, λ is the relativistic wavelength of the electrons (1.97 pm at 300 kV), L is the calibrated camera length in pixels, and R is the number of pixels from the center. L was calibrated by least-squares regression of the calculated d-spacings from the SAD versus published values from the International Centre for Diffraction Data (ICDD). Based on the least-squares fitting for 12 diffraction patterns from seven separate compounds and mixtures independently analyzed by X-ray diffraction, a mean value of 1.92×10^4 pixels for a nominal 370-mm camera length (as reported by the TEM console) was calculated for L. The standard deviation was under 4 parts per thousand [44].

Figures 1 and 2 show this method in practice with a sample of 3DOM iron produced by reducing iron salts in hydrogen. A thin section of this material is shown in the transmission electron micrograph in Fig. 1a–c, with the corresponding SAD pattern shown in Fig. 1d. The dark pointed object from the center right side of Fig. 1d is the beam stop, which was inserted to alleviate saturation of the

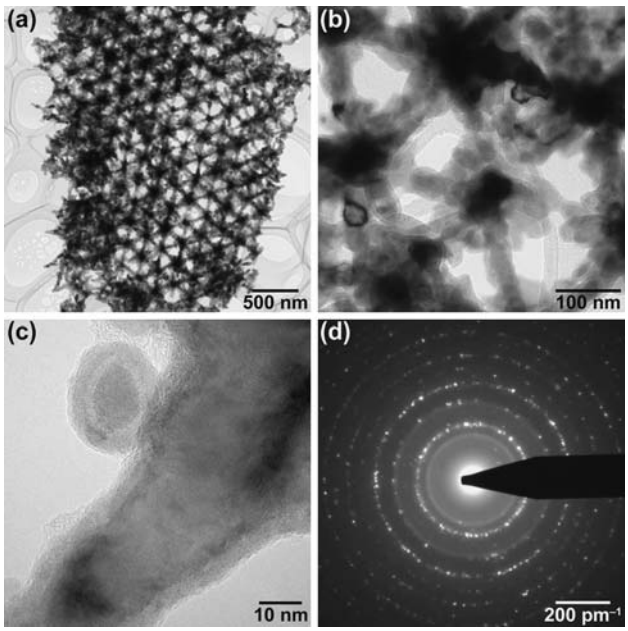

Fig. 1 Bright-field TEM images of 3DOM Fe metal. (**a**) Low-magnification image showing the long-range order and surface defects in the structure. (**b**) Higher-magnification image from the same particle showing the large grain size, relative to 3DOM metal samples produced by direct conversion of the salt in an inert atmosphere. Also visible is the shell-and-core structure of the grains. (**c**) Two of the grains in the same particle at higher magnification, more clearly showing the shell-and-core structure. (**d**) SAD pattern from the same sample that shows both diffuse and sharp, speckled rings. The gamma value of (**d**) has been set to 4 to make visible fainter features in the pattern visible (Image (**c**) is reprinted from [43] with permission. Copyright 2001 American Chemical Society)

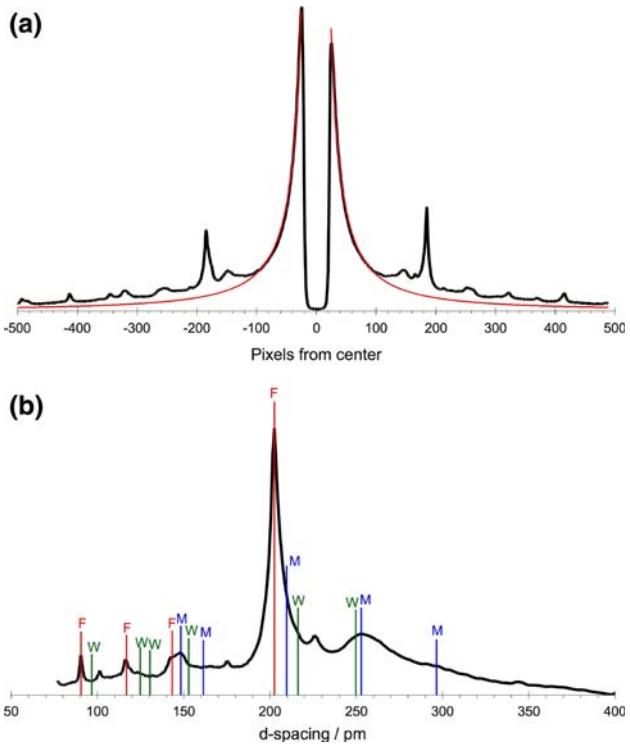

Fig. 2 Phase analysis of 3DOM Fe metal by selected-area electron diffraction (SAD). (**a**) Line profile of a 20-pixel-wide vertical swath of the SAD in Fig. 1d. (**b**) The background-subtracted profile converted into *d*-spacings with phases identified: red/F = α-iron (ferrite), blue/M = magnetite, green/W = wüstite

CCD. A 20-pixel-wide LSP was taken vertically through the center of the diffraction pattern to generate Fig. 2a; the background subtraction used is shown in red ($A = 0.1493$, $B = 1.488$). The large dip in the center of Fig. 2a was caused by the beam stop. In its final form (Fig. 2b), the pattern shows a clear match to α-iron/ferrite (red, powder diffraction file (PDF) no. 6-696) [50] and Fe_3O_4/magnetite (blue, PDF no. 19-629) [51], with several unindexed peaks that probably correspond to distorted or non-stoichiometric FeO/wüstite (green, PDF no. 46-1312) [52]. This phase identification can then be fed back into the bright-field micrograph, showing an iron core surrounded by two distinct oxide layers, which may have formed during handling in air.

Size distribution analyses

The distribution of grain sizes and pore spacings was determined by randomly selecting particles from TEM images and measuring their dimensions in NIH Image 1.63. (For clarity, in this paper these smallest crystalline constituents are called grains and the larger macroporous solids are called particles.) Grains were rejected if they showed indistinct boundaries (usually due to overlap with many other grains or the bars of nickel TEM grid) or truncated by the edge of the micrograph.

Results

High-temperature TEM of 3DOM cobalt

Bright-field TEM images that show the changes in the structure with temperature are presented in Fig. 3. The images from a particle before any heating took place (Fig. 3a–d) show a well-ordered structure composed of tightly arranged grains of cobalt. The bars from the TEM support grid are visible in Fig. 3a as the black triangles in the upper-left and lower-left corners of the image. The *p6mm* plane symmetry of the large 3DOM particle indicated that it was aligned along a [111] zone axis, which corresponds to the close-packed stacking layers of the spherical templates [25]. In the upper-right corner of Fig. 3a is a scrap of porous but less well-ordered cobalt. The light, ovoid structures that appear in the other areas are from the thin holey carbon support film. Higher-magnification images in Fig. 3b and c show small imperfections in the structure, particularly distortions in the pore spacing that have caused the walls not to completely align and to appear as two or three parallel lines in the image. Two of these features are identified with arrows in Fig. 3b. The highest-magnification image at room temperature, Fig. 3d, shows a thin section of wall overlapping a hole in the carbon support film; irregular grains, all less than 10 nm in diameter, were observed in close contact with each other.

When the temperature was raised from room temperature to 500 °C, the structure changed almost immediately: the pore spacing shrank (Fig. 3e, f). The scale on Fig. 3c, e is identical to facilitate comparison and the hexagon is of the same size in both images, but the small tilt makes the actual pore spacing appear larger. At the same time, the wall structure appeared to become more open as the grains composing the structure grew larger (Fig. 3g). At low magnification (Fig. 3e), the structure has noticeably tilted away from the original [111] axis; it was unclear whether this was due to distortions in the 3DOM structure or in the TEM support grid.

The first observation of metal particles apparently suspended in space was made after about 10 min (Fig. 3f–h). At low magnification (Fig. 3f), the dark metal grains appeared to repel each other with a thin, diffracting layer apparently separating the individual grains. Closer observation of these grains showed that they were held together by a web-like structure (Fig. 3h). These webs were observed whether the grains of the particle were in contact with the carbon support film or not (Fig. 3g). No further

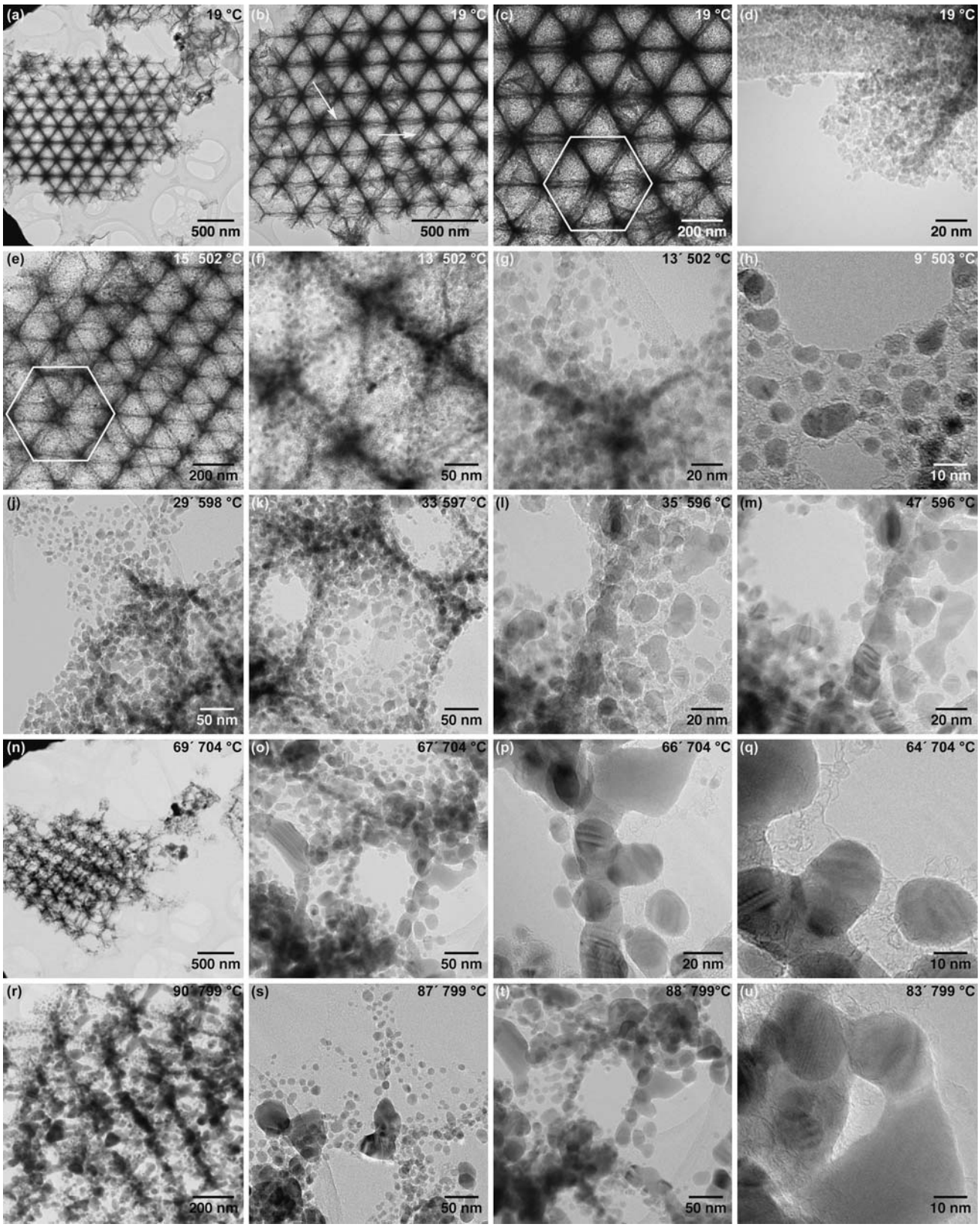
(a) 19 °C
500 nm
(b) 19 °C
500 nm
(c) 19 °C
200 nm
(d) 19 °C
20 nm
(e) 15´ 502 °C
200 nm
(f) 13´ 502 °C
50 nm
(g) 13´ 502 °C
20 nm
(h) 9´ 503 °C
10 nm
(j) 29´ 598 °C
50 nm
(k) 33´597 °C
50 nm
(l) 35´ 596 °C
20 nm
(m) 47´ 596 °C
20 nm
(n) 69´ 704 °C
500 nm
(o) 67´ 704 °C
50 nm
(p) 66´ 704 °C
20 nm
(q) 64´ 704 °C
10 nm
(r) 90´799 °C
200 nm
(s) 87´ 799 °C
50 nm
(t) 88´799°C
50 nm
(u) 83´ 799 °C
10 nm

◀ **Fig. 3** Bright-field TEM images from in situ heating of 3DOM cobalt metal. The temperature recorded on each image is in the value reported by the thermocouple on the holder. Times reported are in minutes from initial heating. The specimen holder temperatures and elapsed times for the images were (**a**–**c**) 19 °C; (**d**–**f**) 0–15 min, 500 °C; (**g**–**j**) 16–51 min, 600 °C; (**k**–**n**) 52–70 min, 700 °C; and (**o**–**r**) 71–95 min, 800 °C. Arrows in (**b**) indicate structural defects. The hexagons in (**c**) and (**e**) are drawn to the same scale to illustrate pore shrinkage

grain growth or particle coarsening was observed until the temperature was raised another 100 °C.

The pore spacing rapidly shrank again when the temperature was raised to 600 °C. The coarsening of the grains at this temperature was notably different: the grains grew at different rates depending on their location within the 3DOM structure. The grains in denser areas of the sample grew much more rapidly than those near the pore windows (Fig. 3j–m). In Fig. 3j, for example, the grains that make up the thin sections of the wall in the upper left of the image remained relatively small, while those in the denser section in the bottom right where the separate walls connected with each other coarsened significantly. The effect was especially evident in the pair of images shown in Fig. 3l, m, which show the same area 12 min apart. Again, the individual grains composing the wall "struts" (running vertically through both images) noticeably coarsen, while the size of the grains further from this strut remain relatively constant in size.

These same trends in grain growth continued to be observed when the sample temperature was raised first to 700 °C (Fig. 3n–q) and then to 800 °C (Fig. 3r–u), except that at higher temperatures the filaments isolating the smaller grains began to break down and the smaller grains were consumed as well. For example, the sample region shown in Fig. 3l, m, as noted in the previous paragraph, is shown again in Fig. 3p, q. Some smaller "island archipelago" grains were still observed even at 800 °C (Fig. 3s), but these may have been supported only by the holey carbon film and not the filaments connecting the grains. The continued twisting or distortion of the particle is evident in Fig. 3n, r; at the highest temperature the particle appears to be nearing a [110] orientation, a rotation of about 35°.

The changes in the pore spacing and grain size are summarized in Table 4. No statistically significant pore-size contraction was observed above 600 °C. Also, the tabular presentation of the grain size data does not adequately represent the changes observed; the particle-size histogram shown in Fig. 4 shows the evolution of the grain size from a single-mode distribution centered on about 6 nm at 19 °C, to a bimodal distribution centered on 15 nm and 42 nm at 800 °C.

The evolution of the SAD pattern with temperature was also significant (Fig. 5). The rings started out diffuse and

Table 4 Changes in pore spacing and average grain size with temperature for 3DOM cobalt

Temp. (°C)	Pore spacing (nm)[a]	N[b]	Grain size (nm)[c]	N[b]
19	524 ± 18	12	6.0 ± 2.3	17
500	397 ± 31	4	9.3 ± 3.8	37
600	315 ± 44	7	14.1 ± 7.6	28
700	292 ± 30	4	22.8 ± 12.5	27
800	338 ± 13	4	25.60 ± 16.0	30

[a] Precision is given as a sample standard deviation (σ_{n-1})

[b] Number of samples

[c] Precision is given as a population standard deviation (σ_n)

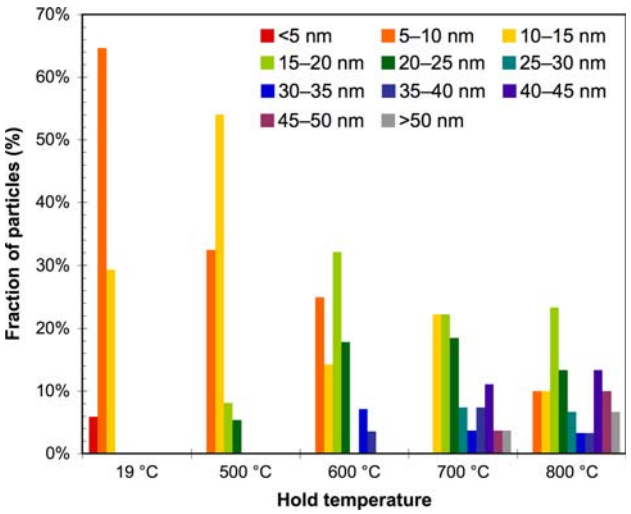

Fig. 4 Grain-size histogram for 3DOM Co metal sample shown in Fig. 3

continuous, then became more speckled and less continuous with increasing time and temperature as the grains coarsened. Analysis of these SAD patterns (Fig. 6) showed the presence of both cubic cobalt(II) oxide (PDF no. 48-1719)[53] and cobalt metal (PDF no. 15-806)[54] at 500 °C; the cobalt(II) oxide disappeared by 600 °C.

High-temperature TEM of 3DOM iron oxide

Nearly the same procedure was used on a calcined sample of 3DOM iron oxide. Figure 7a, b shows a relatively disordered particle at room temperature. The dark circles in the images outline the regions where the template spheres were present in the composite structure. The higher-magnification image (Fig. 7b) showed a wider distribution in grain sizes than there was in the 3DOM cobalt. The walls appeared to have more gaps in between the grains than they did in the 3DOM cobalt. Despite having a more ionic character than cobalt, the iron oxide grains did not show much faceting.

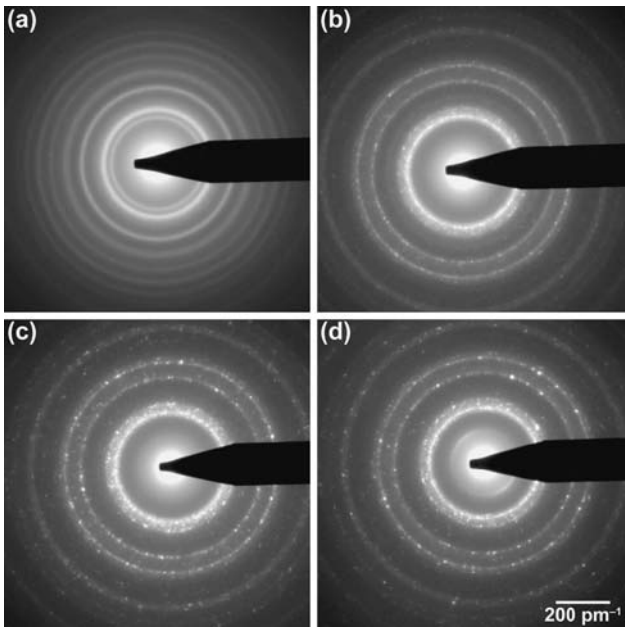

Fig. 5 SAD patterns of 3DOM cobalt taken from the areas shown in Fig. 3 after (**a**) 3 min elapsed time, 500 °C; (**b**) 51 min, 602 °C; (**c**) 94 min, 793 °C; and (**d**) 99 min, 882 °C. The scale is identical for all four SAD patterns. The gamma value for all the images has been set to 4 to make fainter features in the pattern visible

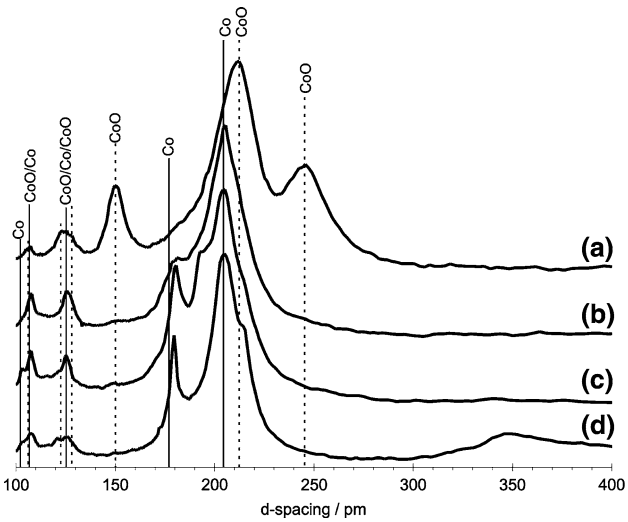

Fig. 6 Analysis of SAD patterns of 3DOM Co metal shown in Fig. 5 converted into *d*-spacings: (**a**) 3 min, 500 °C; (**b**) 51 min, 602 °C; (**c**) 94 min, 793 °C; (**d**) 99 min, 882 °C

As in the case of the 3DOM cobalt, when the 3DOM iron oxide was heated to 650 °C (Fig. 7c–k), the grains grew quickly, and those grains closest to others grew more quickly. The pore windows on this second particle, oriented close to a [111] zone axis, opened up considerably as the smallest grains disappeared. Grains larger than 50 nm were commonly observed at all the wall intersection points (Fig. 7j, k).

By 750 °C, almost all the small grains had been consumed (Fig. 7l, m) with just a few remaining on the "struts." At 950 °C, the framework was composed of large, clearly faceted grains throughout the structure (Fig. 7n–q). The wall intersection points all had grains around 200 nm in diameter, and the walls had all coarsened leaving just a few grains all around 50 nm across.

The distribution of grain sizes (Table 5) was unimodal, unlike the distribution for 3DOM cobalt. Also, there was no statistically significant change in pore size: the hexagons in Fig. 7c, e, j are all drawn to the same scale and each provides the same overlap with the hexagonal projection.

Superficially, the transformation in the SAD pattern with temperature (Fig. 8) from diffuse rings to sharp spots as the iron oxide grains coarsened was similar to the changes observed in Fig. 5. Analysis of these patterns (Fig. 9) revealed that the particle contained both hematite [48] and magnetite [51], even though the PXRD analysis of the as-synthesized product showed only hematite. This transformation is not surprising for a sample in the high-vacuum, electron-rich TEM column: phase diagrams predict a mixture of magnetite and hematite at low oxygen pressures [55–57]. Magnetite was detected even in the room-temperature diffraction patterns (Fig. 9a), showing the {220} and {400} reflections at 297 and 210 pm, respectively.

High-temperature ESEM of 3DOM nickel(II) oxide and its precursor

For further insight into the conversion of the metal salt–latex composite into a 3DOM structure, the transformation of a sample of nickel(II) oxalate in a PS colloidal crystal was studied by high-temperature ESEM. All the images shown in Fig. 10 were taken from the same sample area. The ESEM images were much noisier than the TEM images because of the early model gaseous secondary electron detector in the ESEM.

At room temperature and at 73 °C (Fig. 10a, b), below the glass-transition temperature (T_g, ca. 107 °C, depending on analysis method and composition [58]) for PS, the colloidal crystal array comprises most of the image. In the bottom left of these two images are disordered masses of PS labeled with a "D." The brighter areas, such as those below the scale bars, are due to build-up of residual electrical charge on the insulating surface that was not carried away by ionizing the surrounding gas [59, 60]. These "hot spots" occurred less often as the spheres melted and became less textured, and as the higher sample temperature allowed for more efficient removal of excess charge.

By 125 °C, just above the T_g of PS, small parts of the sample in closest contact with the alumina crucible began to melt: the edges of the template material in the upper left

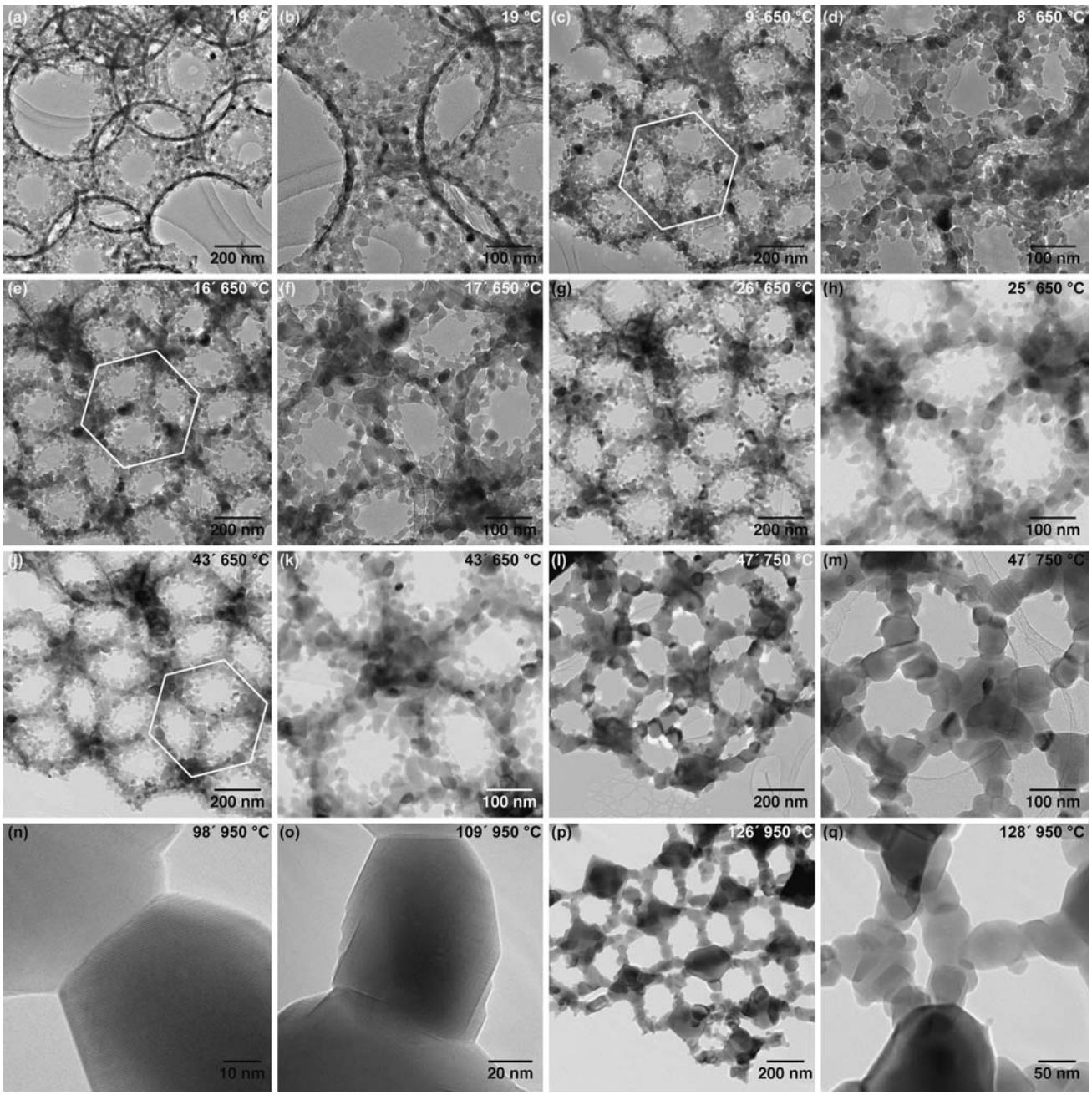

Fig. 7 Bright-field TEM images from in situ heating of 3DOM iron oxide. The temperature recorded on each image is in the value reported by the thermocouple on the holder. The specimen holder temperatures and times, reported are in minutes from the first heating step, are: (**a**) and (**b**), 19 °C; (**c**–**k**), 650 °C, 9–45 min; (**l**) and (**m**), 750 °C, 47 min; and (**n**–**q**), 950 °C, 98–128 min. The hexagons in (**c**, **e,** and **j**) are drawn to the same scale

of Fig. 10c (labeled "M") became less distinct. The rest of the structure remained relatively unperturbed because of the low thermal conductivity of the sample and low convective heat transfer at the operating pressure of ~0.6 kPa. By the time the temperature was raised to over 200 °C (Fig. 10d), a much greater fraction of the sample had melted. Despite this, the top-most parts of the colloidal crystals still showed distinct individual spheres after an additional 20 min (Fig. 10e).

The colloidal crystal structure entirely disappeared only after the temperature was ramped to over 400 °C (Fig. 10f), and then the melted polymer spread out and began to decompose (Fig. 10g). By nearly 90 min, the first bits of 3DOM product began to appear at the surface of the

Table 5 Changes in pore spacing and average grain size with temperature for 3DOM iron oxide

Temp. (°C)	Pore spacing (nm)[a]	N[b]	Grain size (nm)[c]	N[b]
19	524 ± 9	7	16.4 ± 7.6	20
650	435 ± 16	18	25.4 ± 9.6	64
750	450 ± 8	12	54.6 ± 40.4	28
950	513 ± 13	5	78.5 ± 38.1	22

[a] Precision is given as a sample standard deviation (σ_{n-1})

[b] Number of samples

[c] Precision is given as a population standard deviation (σ_n)

PS melt. In Fig. 10g, these are most visible in the upper-right quarter of the image, where evenly spaced, uniformly sized dark circles in light rings can be differentiated from the relatively uniform background. Two other examples are circled in Fig. 10g.

The relatively flat, melted polymer continued to decompose with time. The first tears or cracks appeared in the degraded precursor just under 2 h from the start of the heating, with the 3DOM "skeletons" emerging from the melt (Fig. 10h–k). The white arrows in Fig. 10h–m point to the same cluster of particles. After about 2.5 h, the coarse-grained alumina crucible was visible (labeled "C"), at first around the edges of the 3DOM particles (e.g., in the upper right of Fig. 10l) then all around them. The heating was stopped after 3 h, when all the PS had decomposed and only the 3DOM product was visible. The 3DOM product was not observed to change further at the resolution of the ESEM.

The product could not be isolated after the ESEM work for further analysis in a TEM or higher-resolution SEM to provide better images of the structure and to determine the product's composition (i.e., whether it formed a metal or an oxide product).

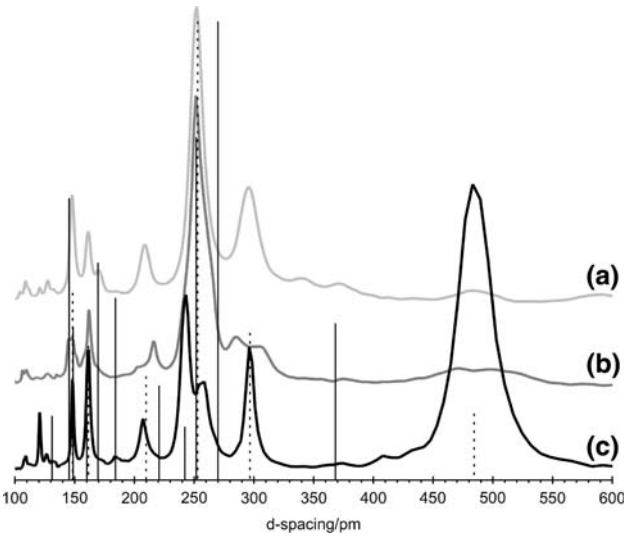

Fig. 9 Analysis of SAD patterns of the 3DOM iron oxide shown in Fig. 8 converted into *d*-spacings. (**a**) 19 °C, (**b**) 650 °C, (**c**) 750 °C. Solid lines correspond to the *d*-spacings of hematite, dotted lines correspond to those of magnetite

Discussion

A key discovery from the high-temperature TEM investigation is the role of intrinsic carbon in limiting the grain growth, as observed in the 3DOM cobalt metal sample. As noted in the experimental section, elemental analysis showed that about one-fifth of the mass of the 3DOM cobalt was carbon, so at first it appears remarkable that there was no evidence of a graphitic carbon shell in even the thin segment of pore wall shown at high magnification in Fig. 3d; lattice fringes associated with graphitic carbon that remained from incomplete decomposition of the PMMA template in 3DOM materials have previously been observed in 3DOM nickel and 3DOM cobalt [43, 44]. However, an estimate that assumes bulk densities and spherical 6-nm diameter grains of cobalt coated with a

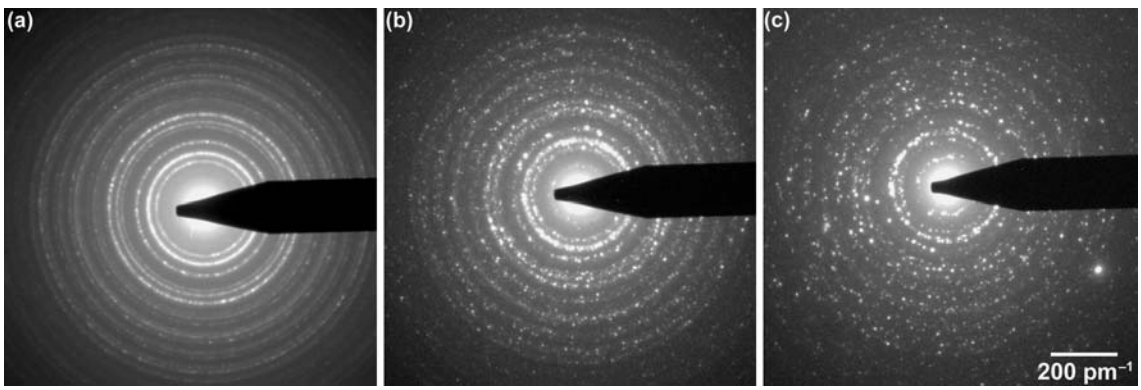

Fig. 8 SAD patterns of 3DOM iron oxide taken from the areas shown in Fig. 7 recorded at (**a**) 19 °C, (**b**) 650 °C, and (**c**) 750 °C. The scale is identical for all three SAD patterns. The gamma value for these images has been set to 4 to make fainter features in the pattern visible

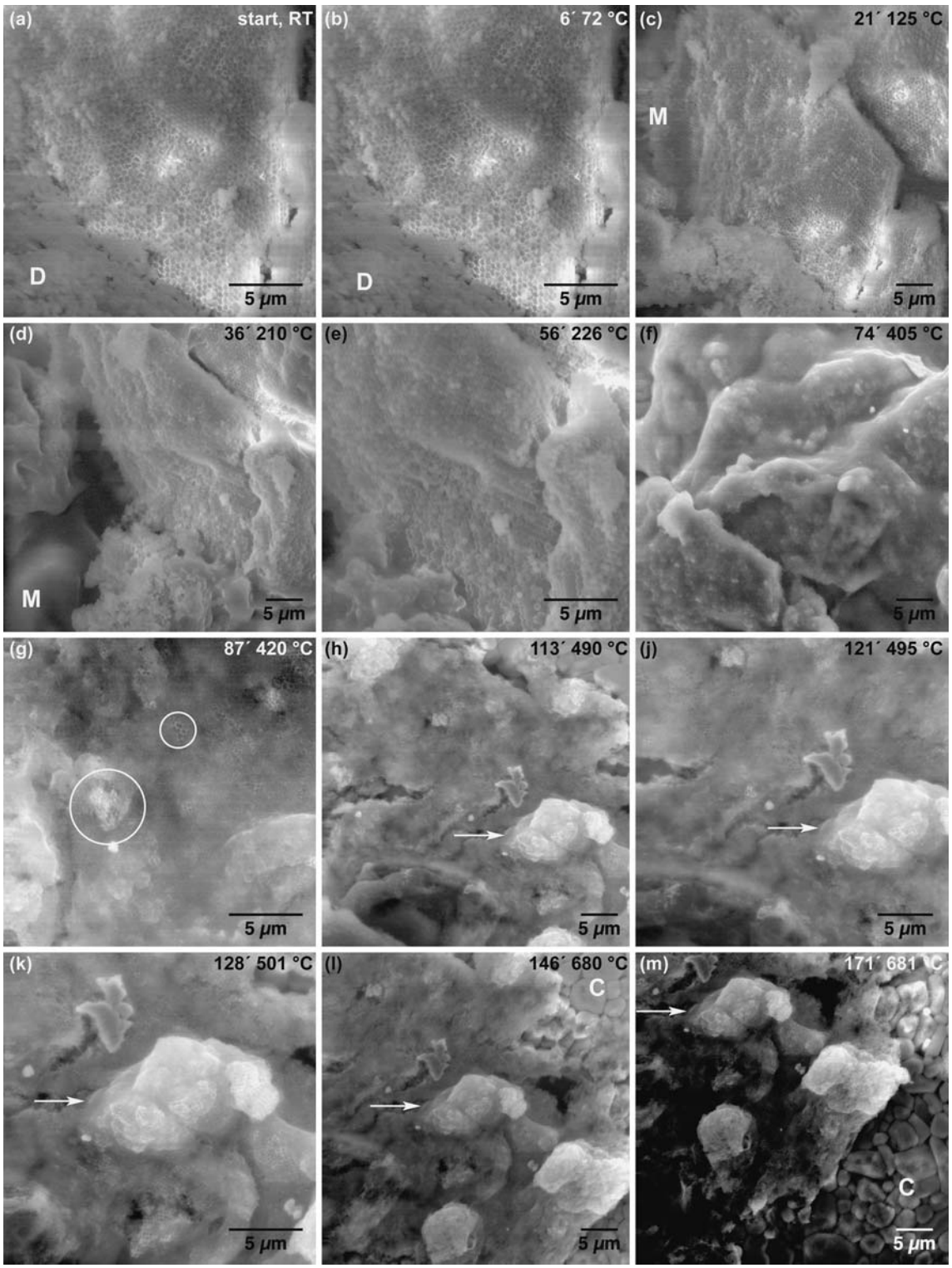

Fig. 10 Secondary electron ESEM images showing the decomposition of the latex from a nickel(II) oxalate–PS latex composite. All images are taken from the same group of particles. The letters on the images denote the following: D, disordered region of precursor; M, melted precursor; C, crucible. The circles highlight two areas in (**g**) where the 3DOM product is emerging from the decomposing precursor. The arrows point to the same cluster of particles in images (**h**–**m**)

uniform carbon shell produces an average shell thickness of just 0.78 nm to give the measured carbon mass fraction. This corresponds closely to the thickness between single planes of graphite (0.67 nm), suggesting that the grains may be coated with only a single carbon layer that was obscured by the imaging conditions.

The carbon fibers observed in Fig. 3h appeared to be limiting the mass transfer between grains to permit their coalescence. The smaller grains in the 3DOM cobalt discussed in this paper were those that were isolated from the denser sections by the fibers of the structure, while the larger grains were closer to other grains and grew by consuming the smaller grains around them to minimize surface area (Ostwald ripening). The contrasting structural evolution of the 3DOM iron oxide, which had no carbon left in it, supports this hypothesis of the carbon acting to limit diffusive mass transport between grains.

The presence of cobalt oxide in the room-temperature SAD pattern (but not in the room-temperature PXRD pattern [43]) suggests that the carbon in the sample either did not completely surround the grains or that it did not provide a complete barrier to oxygen. The oxide is more likely to have disappeared by reaction with surface carbon to produce carbon monoxide or carbon dioxide than by sublimating into the vacuum. The reaction producing carbon monoxide becomes thermodynamically favorable at about 500 °C, and the reaction producing carbon dioxide becomes favorable at about 250 °C [61], whereas the vapor pressure of cobalt(II) oxide and its dissociation products are all orders of magnitude lower than the column pressure of the TEM [62]. The reduction of the cobalt oxide by 500 °C in the vacuum of the TEM column did not cause a noticeable structural change. The decomposition of the carbon capsules, however, may largely account for the 3DOM cobalt shrinkage between room temperature and 500–600 °C, with no statistically significant shrinkage at higher temperatures. This hypothesis is supported by the lack of shrinkage in the 3DOM iron oxide.

The observations from heating under high-vacuum conditions in the TEM obviously do not directly correspond to the behavior of these materials in an environment where oxidation and convective heat transfer play significant roles. However, the high-temperature TEM observations illustrate the notable effect of carbon encapsulation on the microstructural evolution of 3DOM materials. Carbon coatings restricting grain growth have previously been noted in lithium iron phosphate cathode materials [63], sintering of zirconium diboride powders [64] and, most relevantly, the sintering of nickel and cobalt nanocrystals studied by Host and co-workers [65]. As in this work, Host et al. did not observe the formation of any carbides or metal–carbon solid solutions by PXRD. Carbon has also been observed to enhance the stability of the microstructure of electrodeposited, nanocrystalline nickel at temperatures below about 500 °C [66], noting a bimodal distribution in grain sizes upon heating which later researchers attributed to a wetting, sulfur-rich phase that formed at the growth interfaces [67].

Also, the TEM results showed that temperature rather than time plays the more consequential part in the grain growth kinetics: in both cases, the grain size reached a plateau at each temperature at which point grain growth effectively ceased until the temperature was raised again. This observation suggests that diffusive transport rather than addition of atoms to the interface is the rate-limiting step in grain growth. This behavior is surprising in the case of the faceted 3DOM iron oxide, where there is a larger energetic penalty for adding atoms to the flat surface; this penalty may be balanced by the high surface-to-volume ratio of the nanoparticles [68]. Molecular dynamics simulation of small clusters of copper and gold nanoparticles, studied as isolated virtual particles rather than bulk materials, produced similar effects to those seen in the late-stage 3DOM cobalt growth (e.g., Fig. 3u), including the incorporation of smaller grains into larger ones and the formation of curved necks around particle interfaces [69]. The authors concluded that surface diffusion and grain-boundary diffusion were the dominant mass transport mechanisms, consistent with the stabilizing role of surface carbon. In contrast to qualitative match to the 3DOM cobalt results, however, the faceted interfaces of 3DOM iron oxide (shown most clearly in Fig. 7n) resisted necking, illustrating the complicating influence of stable, low-energy surfaces on models of sintering and grain growth.

The variable-temperature ESEM analysis of the nickel(II) oxalate–PS sample allowed the conversion to be monitored at a fine scale. The shrinkage that occurs when calcining 3DOM materials prepared by salt infiltration has previously been measured by comparing the size of the latex sphere templates to the pore spacing in the 3DOM product [2, 4, 5], but had never been observed directly.

A calcination process that is identical to the one routinely used to produce 3DOM materials is impossible to create in the ESEM. Although some oxygen was present during these time and temperature studies, it was still 30–40 times lower than the partial pressure of oxygen present in air. In addition, the total pressure inside the ESEM sample chamber was more than 100 times less than atmospheric, which would be expected to give lower heat transport (because of the relative absence of convective processes) and lower transport of decomposition products from the surface. Finally, the displayed temperatures appeared somewhat high based on observations of the decomposition of PS in air. The skew in the temperature scale may be due to the thermocouple being located nearer to or in better thermal contact with the heating element than the sample.

Conclusions

Despite the limitations imposed by operating under vacuum, both high-temperature techniques gave new insights into the processing of 3DOM materials. From the HT-TEM

work, a maximum working temperature for a 3DOM material can be established by setting an upper limit on the grain size (usually 10–100 times smaller than the operating wavelength for photonic applications). In addition, the technique gave a clear demonstration of carbon slowing the grain growth or coarsening of nanoparticulate metal. The ability to identify crystalline phases easily while following morphological changes makes in situ HT-TEM well suited for further studies on 3DOM and other photonic band gap materials.

HT ESEM should prove valuable for following the final, template removal stage in the synthesis of 3DOM materials. One possible use is in the assessment of precursor infiltration efficiency. As ESEM imaging systems improve, clearer and higher-resolution images should be more readily obtained. This should greatly aid the optimization of the synthesis of 3DOM materials as well as other template-based structures.

Acknowledgements The authors thank Dr. Hongwei Yan for providing the samples of 3DOM materials, Dr. Stuart McKernan for assistance with the ESEM and TEM, and the David and Lucile Packard Foundation and the 3M Heltzer Endowed Chair of the University of Minnesota for research funding.

References

1. Velev OD, Jede TA, Lobo RF, Lenhoff AM (1997) Nature 389:447
2. Holland BT, Blanford CF, Stein A (1998) Science 281:538
3. Wijnhoven JEGJ, Vos WL (1998) Science 281:802
4. Lytle JC, Stein A (2006) In: Cao G, Brinker CJ (eds) Annual reviews of nano research. World Scientific Publishing, Hackensack, NJ, pp 1
5. Stein A, Li F, Denny NR (2008) Chem Mater 20:649
6. Blanford CF, Yan H, Schroden RC, Al-Daous M, Stein A (2001) Adv Mater 13:401
7. Schroden RC, Al-Daous M, Blanford CF, Stein A (2002) Chem Mater 14:3305
8. Joannopoulos JD, Meade RD, Winn JN (1995) Photonic crystals: molding the flow of light. Princeton University Press, Princeton
9. Beck JS, Vartuli JC, Roth WJ, Leonowicz ME, Kresge CT, Schmitt KD, Chu CT-W, Olson DH, Sheppard EW, McCullen SB, Higgins JB, Schlenker JL (1992) J Am Chem Soc 114:10834
10. Sing KSW, Everett DH, Haul RAW, Moscou L, Pierotti RA, Rouquerol J, Siemieniewska T (1985) Pure Appl Chem 57:603
11. van Bekkum H, Flanigen EM, Jansen JC (1991) Introduction to zeolite science and practice. Elsevier, Amsterdam
12. Huo Q, Margolese DI, Stucky GD (1996) Chem Mater 8:1147
13. Luck W, Klier M, Wesslau H (1963) Ber Bunsen Phys Chem 67:75
14. Clark NA, Hurd AJ, Ackerson BJ (1979) Nature 281:57
15. Yan H, Blanford CF, Holland BT, Smyrl WH, Stein A (2000) Chem Mater 12:1134
16. Subramania G, Constant K, Biswas R, Sigalas MM, Ho KM (1999) Appl Phys Lett 74:3933
17. Blanco A, Chomski E, Grabtchak S, Ibisate M, John S, Leonard SW, López C, Meseguer F, Míguez H, Mondia JP, Ozin GA, Toader O, van Driel HM (2000) Nature 405:437
18. King JS, Gaillot DP, Graugnard E, Summers CJ (2006) Adv Mater 18:1063
19. Caruso F, Caruso RA, Möhwald H (1998) Science 282:1111
20. John S (1987) Phys Rev Lett 58:2486
21. Yablonovitch E (1987) Phys Rev Lett 58:2059
22. Megens M, Vankats CM, Bosecke P, Vos WL (1997) J Appl Crystallogr 30:637
23. Vos WL, Megens M, Vankats CM, Bosecke P (1997) Langmuir 13:6004
24. Vos WL, Sprik R, van Blaaderen A, Imhof A, Lagendijk A, Wegdam GH (1996) Phys Rev B 53:16231
25. Blanford CF, Carter CB, Stein A (2004) J Microsc Oxford 216:263
26. Schroden RC, Stein A (2004) In: Caruso F (ed) Colloids and colloid assemblies: synthesis, modification, organization and utilization of colloid particles. Wiley VCH, Weinheim, Germany, pp 465
27. Mittleman DM, Bertone JF, Jiang P, Hwang KS, Colvin VL (1999) J Chem Phys 111:345
28. Anderson MW, Ohsuna T, Sakamoto Y, Liu Z, Carlsson A, Terasaki O (2004) Chem Commun 907
29. Kamino T, Yaguchi T, Konno M, Hashimoto T (2005) J Electron Microsc 54:461
30. Akita T, Tanaka K, Kohyama M, Haruta M (2007) Catal Today 122:233
31. Yoshida R, Suzuki Y, Yoshikawa S (2005) Mater Chem Phys 91:409
32. Setoyama M, Irie M, Ohara H, Tsujioka M, Takeda Y, Nomura T, Kitagawa N (1999) Thin Solid Films 341:126
33. Lee J, Lee J, Tanaka T, Mori H, Penttila K (2005) JOM-J Min Met Mat S 57:56
34. Lee JG, Mori H (2004) Philos Mag 84:2675
35. Gai PL, Calvino JJ (2005) Ann Rev Mater Res 35:465
36. Gai PL, Kourtakis K (1995) Science 267:661
37. Meller N, Hall C, Crawshaw J (2004) J Mater Sci 39:6611
38. Meredith P, Donald AM, Meller N, Hall C (2004) J Mater Sci 39:997
39. Baranov AN, Chang CH, Shlyakhtini A, Panin GN, Kang TW, Oh YJ (2004) Nanotechnology 15:1613
40. Siriwardane RV, Poston JA, Fisher EP (2005) Appl Surf Sci 243:40
41. Holland BT, Blanford CF, Do T, Stein A (1999) Chem Mater 11:795
42. Yan H, Blanford CF, Holland BT, Parent M, Smyrl WH, Stein A (1999) Adv Mater 11:1003
43. Yan H, Blanford CF, Lytle JC, Carter CB, Smyrl WH, Stein A (2001) Chem Mater 13:4314
44. Blanford CF (2000) Ph.D. Dissertation, University of Minnesota, Twin Cities
45. Goodwin JW, Hearn J, Ho CC, Ottewill RH (1973) Br Polym J 5:347
46. Goodwin JW, Ottewill RH, Pelton R, Vianello G, Yates DE (1978) Br Polym J 10:173
47. Tanrisever T, Okay O, Sönmezoglu IÇ (1996) J Appl Polym Sci 61:485
48. Sawada H (1996) Mater Res Bull 31:141
49. Williams DB, Carter CB (1996) Transmission electron microscopy: a textbook for materials science. Plenum Press, New York
50. Hull AW (1917) Phys Rev 10:661
51. Sasaki S (1997) Acta Cryst B53:762
52. Fjellvag H, Gronvold F, Stolen S, Hauback B (1996) J Solid State Chem 124:52
53. Tombs NC, Rooksby HP (1950) Nature 165:442
54. Hull AW (1921) Phys Rev 17:571
55. Darken LS, Gurry RW (1946) J Am Chem Soc 68:798
56. Phillips B, Muan A (1960) J Phys Chem 64:1451

57. Presnall DC (1995) In: Ahrens TJ (ed) Mineral physics and crystallography: a handbook of physical constants. American Geophysical Union, Washington, DC, pp 248
58. Rieger J (1996) J Them Anal Calorim 46:965
59. Cazaux J (2004) Microsc Microanal 10:670
60. Moncrieff DA, Robinson VNE, Harris LB (1978) J Phys D Appl Phys 11:2315
61. Lide DR (ed) (1996) CRC handbook of chemistry and physics. CRC Press, Ann Arbor
62. Grimley RT, Burns RP, Inghram MG (1966) J Chem Phys 45:4158
63. Yang MR, Teng TH, Wu SH (2006) J Power Sources 159:307
64. Zhu SM, Fahrenholtz WG, Hilmas GE, Zhang SC (2007) Mater Sci Eng A Struct 459:167
65. Host JJ, Block JA, Parvin K, Dravid VP, Alpers JL, Sezen T, LaDuca R (1998) J Appl Phys 83:793
66. Xiao C, Mirshams RA, Whang SH, Yin WM (2001) Mater Sci Eng A Struct 301:35
67. Hibbard GD, McCrea JL, Palumbo G, Aust KT, Erb U (2002) Scripta Mater 47:83
68. Carter CB, Norton MG (2007) Ceramic materials: science and engineering. Springer-Verlag, New York
69. Zeng P, Zajac S, Clapp PC, Rifkin JA (1998) Mater Sci Eng A Struct 252:301